Analyst

PAPER

View Article Online
View Journal | View Issue

Cite this: *Analyst*, 2025, **150**, 5245

A multifunctional probe for optical and electrochemical detection of hydrogen sulfide and real-time selective fungal imaging

Ranjana M.,[a] Namita N. Kashyap,[b] Dhanya Sunil, *[a] Anshuman Bera,[c] Prajoy Kumar Mitra, [c] Prakash Peralam Yegneswaran,[d] Sudhakar Y. N., [a] Dinesh Upadhya,[b] Suresh D. Kulkarni [e] and Sivaranjana Reddy Vennapusa [c]

This study reports the synthesis of 2-hydroxy-*N*-(6-nitro-1,3-dioxo-1*H*-benzo[*de*]isoquinolin-2(3*H*)-yl) benzamide (SNN), designed for the selective detection of hydrogen sulfide (H_2S) and real-time imaging of *Candida albicans*. The probe was synthesized *via* imidation of 4-nitronaphthalic anhydride with salicyl hydrazide, leveraging the environmentally responsive fluorescence properties of naphthalimide derivatives. SNN demonstrated dual-mode functionality, enabling both optical and electrochemical sensing of H_2S across a range of pH conditions, thereby providing insights into sulfur chemistry. Remarkably, SNN allowed direct wet-mount imaging of *C. albicans* without the need for prolonged incubation, producing high-contrast fluorescence with minimal background noise *via* endogenous H_2S activation. It showed selective nuclear localization in *C. albicans* but did not facilitate fluorescence imaging in *Aspergillus niger*. Additionally, SNN was used for effective visualization of other fungi associated with bread spoilage, highlighting its promise as a versatile tool for fungal diagnostics and food safety applications. Moreover, the H_2S-specific imaging was validated through incubation studies using 2-(aminooxy)acetic acid hydrochloride, a selective inhibitor of the cystathionine beta-synthase enzyme involved in the production of H_2S and the metabolism of homocysteine.

Received 25th July 2025,
Accepted 3rd October 2025

DOI: 10.1039/d5an00783f

rsc.li/analyst

1. Introduction

Fungal infections coupled with the rapid emergence of drug resistance pose a grave threat to human health, especially in immunocompromised individuals, and cause more than a million deaths annually.[1] Redox homeostasis is essential for host colonization by fungal pathogens such as *Candida albicans*. Hydrogen sulfide (H_2S), once regarded solely as a hazardous, colorless, and flammable gas with a characteristic rotten egg odor, is now recognized as a crucial gaseous signaling molecule in both mammals and microbes.[2] This paradigm shift stems from its emerging role in regulating diverse physiological and pathological processes.[3,4] In fungi, H_2S is generated from cysteine degradation, sulfate reduction, and transsulfuration through both enzymatic and non-enzymatic reactions. H_2S production in fungi is a known phenomenon, although it is not common in all species.[5,6] Research has shown that yeasts such as *Saccharomyces cerevisiae* and *C. albicans* can produce endogenous H_2S enzymatically through the catabolism of amino acids (*S*-propargyl-cysteine) or the utilization of the cystathionine β-synthase (CBS) enzyme.[7–9] In *C. albicans*, the *CYS4* gene is annotated in the Candida Genome Database as encoding CBS, which is responsible for H_2S biosynthesis.[8] Besides, polysulfides and glutathione (GSH) could be converted to H_2S *via* a non-enzymatic pathway.[10] H_2S is more than just a byproduct in fungi; it is a biologically active molecule involved in metabolism, redox balancing, sulfur homeostasis, signaling, stress response, promoting survival under stress, morphogenesis, biofilm formation, and possibly virulence.[11] This gaseous molecule is also involved in the production of malformin, a phytotoxic peptide containing D-cysteine,[12] in pathogenic fungi.

Conventional H_2S gas sensors, including electrochemical, semiconductor metal oxide, and printed nanomaterial-based devices, offer high sensitivity[13] and are widely used in environ-

[a]*Department of Chemistry, Manipal Institute of Technology, Manipal Academy of Higher Education, Manipal-576104, Karnataka, India.*
E-mail: dhanyadss3@gmail.com, dhanya.s@manipal.edu
[b]*Centre for Molecular Neurosciences, Kasturba Medical College Manipal, Manipal Academy of Higher Education, Manipal-576104, Karnataka, India*
[c]*School of Chemistry, Indian Institute of Science Education and Research, Thiruvananthapuram-695016, Kerala, India*
[d]*Department of Microbiology, Kasturba Medical College Manipal, Manipal Academy of Higher Education, Manipal-576104, Karnataka, India*
[e]*Manipal Institute of Applied Physics, Manipal Academy of Higher Education, Manipal, 576104 Karnataka, India*

mental monitoring, industrial safety, and medical diagnostics. However, their application in complex biological systems is constrained by challenges such as miniaturization, aqueous compatibility, and biocompatibility. In this context, fluorescence imaging has significantly contributed to our greater understanding of the pathogenic mechanisms of endogenous commensal fungi such as *C. albicans*. As an opportunistic pathogen, it is a major cause of candidemia affecting the blood, with a high mortality rate of ~40%.[14] Microscopic imaging is critical for exploring its virulence and improving diagnostics; however, challenges remain. These include poor adhesion of fungal cells to imaging substrates, thereby complicating confocal microscopy imaging,[15] and extensive autofluorescence. Moreover, limitations including non-specific binding, background staining, photobleaching, and cytotoxicity of commonly used fluorophores, such as calcofluor white, fluorescein isothiocyanate, and 4′,6-diamidino-2-phenylindole, restrict their utility, particularly in live-cell imaging. Addressing these imaging challenges is essential for better visualization of fungal structures, enhancing diagnostic precision and developing more effective therapeutic strategies. Therefore, there is a growing need for less toxic, cell-permeable, and deep-tissue-penetrating probes that can selectively label fungal structures.

Small-molecule fluorescent probes have gained significant attention over traditional methods due to their inherent advantages, including exceptional selectivity, high sensitivity, real-time monitoring, non-destructive visualization, and convenient handling.[16–21] Numerous fluorescent probes have been developed for H_2S gas detection utilizing various strategies, such as the reduction of azides and nitro compounds to amines, Michael addition reactions, H_2S-specific disulfide bond cleavage, nucleophilic and thiolysis reactions, as well as H_2S-induced metal displacement and metal indicator displacement approaches.[22–27] These probes enable imaging of H_2S in living cells, tissues, and blood samples *in vivo*, even allowing for subcellular organelle-targeted analysis. Although there are a few widely used fluorophores, notable advancements have not been made for fungal imaging. H_2S-responsive fluorescent probes offer a novel, selective, and real-time imaging method to detect and study fungi. These probes exploit the endogenous production of H_2S in fungi to emit a measurable fluorescence signal, enabling live-cell imaging, diagnostics, and monitoring of fungal contamination in biological and food systems. Except for a recent study by Yan *et al.* using a thiol-responsive 2,4-dinitrophenyl-based fluorescent probe for the selective detection of endogenous H_2S in fungal cells, there are no other studies reported on the real-time imaging of *C. albicans* that offer insights into the role of H_2S in fungal pathogenicity.[4] In the present study, a new salicyl hydrazide integrated nitronaphthalimide, 2-hydroxy-*N*-(6-nitro-1,3-dioxo-1*H*-benzo[*de*]isoquinolin-2(3*H*)-yl)benzamide (SNN), was designed and synthesized as a multifunctional probe capable of dual-mode detection of H_2S—optical and electrochemical, while also serving as a robust H_2S-based imaging agent for fungal visualization without any prolonged incubation procedures.

2. Experimental

2.1 Materials

4-Nitro-1,8-naphthalic anhydride, salicyl hydrazide, sodium sulfide (Na_2S : H_2S releasing agent), disodium hydrogen phosphate, potassium phosphate monobasic, and sodium chloride were procured from Sigma Aldrich. 2-(Aminooxy)acetic acid hemihydrochloride was purchased from BLD Pharmatech. Solvents, including ethanol, acetone, and dimethyl sulfoxide (DMSO), were obtained from SRL Chemicals. All reagents used were of analytical grade. The phosphate-buffered saline (PBS) solutions of different pH values were prepared using suitable capsules purchased from Merck in Milli-Q water.

2.2 Synthesis and structural characterization of 2-hydroxy-*N*-(6-nitro-1,3-dioxo-1*H*-benzo[*de*]isoquinolin-2(3*H*)-yl) benzamide (SNN)

4-Nitro-1,8-naphthalic anhydride (30 mg, 0.1233 mmol) and salicyl hydrazide (22.5 mg, 0.1479 mmol) in ethanol (5 mL) were refluxed for 10 h under stirring conditions and allowed to cool down to room temperature (Scheme 1). The precipitate formed was filtered, washed with distilled water, and dried at room temperature for 48 h to obtain SNN.

^1H and ^{13}C NMR spectra were recorded on a Bruker Ascend 400 MHz spectrometer, acquired over 16 and 1024 scans, respectively. Approximately 5 mg of SNN was dissolved in 0.4 mL of DMSO-d_6 for recording ^1H NMR spectra, while 10 mg of SNN was used for recording ^{13}C NMR spectra. The IR spectrum of solid SNN was obtained using Shimadzu IR Spirit (Japan) equipment. The mass spectrum (MS) was recorded using a Gas Chromatography-Mass Spectrometer (GC-MS QP2010 Ultra). The mass of reduced SNN was analyzed with a MALDI-TOF Mass Spectrometer (Ultraflextreme, Bruker), which operates in both linear and reflectron ionization modes.

2.3 Theoretical studies

Theoretical calculations were performed using the Gaussian 16 software package[28] with density functional theory (DFT). To obtain the ground state equilibrium geometry (S_0) of SNN and reduced SNN, the CAM-B3LYP/6-311G(d,p) level of theory was used using the universal solvation model density (SMD) in water medium. Furthermore, the same level of theory was

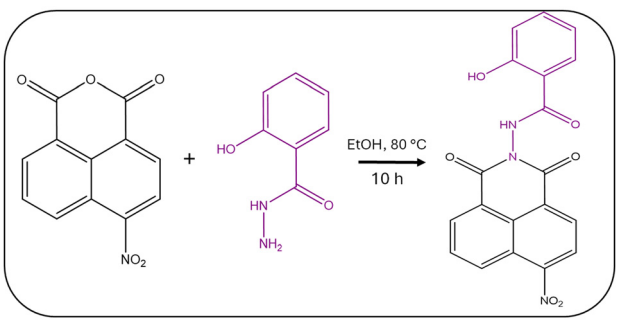

Scheme 1 Synthetic route for SNN.

employed to determine the HOMO–LUMO energy gap and binding energies.

2.4 Electrochemical measurements

Cyclic voltammetry (CV) and square wave voltammetry (SWV) were conducted using a Biologic SP50-e instrument. SWV was performed in the potential window of −2 to 2 V at a scan rate of 100 mV s^{-1}, whereas CV was performed in the potential window of −1.2 to 0.4 V at a scan rate of 5 mV s^{-1}. A three-electrode system was used for voltammetric measurements, comprising a platinum foil as the counter electrode, a silver/silver chloride (Ag/AgCl/KCl (sat.)) electrode as the reference electrode, and a stainless-steel plate (1 cm × 1 cm) as the working electrode. About 0.75 mg of SNN was dissolved in 0.5 mL of DMSO, diluted to 20 mL (1 : 40) using PBS, and used as the electrolyte. Buffer solutions of pH = 3, 7.4, and 9 were used for the study. A stock solution (0.1 M) of Na_2S was prepared in distilled water. CV curves were recorded at 10 mV s^{-1}, and SWV curves were recorded at 10 Hz, with a pulse amplitude of 25 mV, a step potential of 0.5 V, and a scan rate of 100 mV s^{-1} across pH 3–9. A minimum of three individual experiments were performed, and all measurements were conducted at ambient temperature (23 ± 3 °C).

2.5 X-ray photoelectron spectroscopy (XPS) analysis

The XPS measurements were conducted using a Thermo Fisher Scientific Nexsa Base equipped with a K-alpha source, and the data were processed using a self-consistent fitting approach in CasaXPS software. All high-resolution spectra were calibrated to the aliphatic carbon peak at 284.5 eV, ensuring internal consistency.

2.6 Optical studies

For absorption and emission studies, 3.77 mg of SNN was dissolved in 0.5 mL of DMSO and then diluted with PBS (pH 7.4) to prepare a stock solution of 1000 μM. Further dilution of this stock solution was done using PBS to obtain a 100 μM working solution (0.25% DMSO : 99.75% PBS). Emission studies at pH 3 and 9 were conducted by preparing similar dilutions using PBS adjusted to the respective pH values. A stock solution of 0.1 M Na_2S was prepared in distilled water for optical measurements. The stock solutions for selectivity studies were prepared as follows: 100 μM Na_2S (slightly higher concentration to account for *in situ* H_2S generation) and 60 μM each for GSH and cysteine (Cys) and several biologically relevant metal salts including $ZnCl_2$, $MgSO_4$, $CaCl_2$, $AlCl_3$, $CuCl_2$, $FeCl_3$, and $HgCl_2$. Absorbance measurements were carried out using a Shimadzu UV-visible spectrophotometer 2201 with a bandwidth of 3.0 nm, a scan wavelength range of 200–800 nm, and a medium scan speed. A JASCO spectrofluorometer FP-8300 was used to detect fluorescence at excitation wavelengths of 365 and 430 nm. Time-correlated single photon counting (TCSPC) measurements were carried out in Horiba Datastation V2.5, Nano-LED-440L with a pulse duration of <100 ps. Colorimetric studies were carried out using a Systronics Photoelectric Colorimeter with a 430 nm filter. A minimum of three individual experiments were performed for each test.

2.7 Biological studies

2.7.1 Cytotoxicity assay. Human embryonic kidney cells (HEK293T) were cultured in Dulbecco's modified Eagle's medium (DMEM: Thermo Fisher 11965092), supplemented with 10% fetal bovine serum (FBS: RM9955-Himedia), and incubated at 37 °C in 5% CO_2 for 24 h. To evaluate the cytotoxicity of SNN, 5000 cells per well were seeded into 96-well plates and incubated overnight. The cells were then treated with various concentrations of SNN (5–25 μM in 0.01% DMSO and 99.99% DMEM) and incubated for 48 h. Triplicates were maintained for each well. Furthermore, the medium was removed, the cells were exposed to a 3-(4,5-dimethylthiazol-2-yl)-2,5-diphenyltetrazolium bromide (MTT: 0.5 mg mL^{-1}) solution, and incubated for 4 h. The supernatant was discarded, and 200 μL of DMSO was added to each well. Absorbance was measured at 570 nm using a BioTek Synergy H1 microplate reader, and the cell viability percentage was calculated using the following formula: percentage cell viability = OD sample/OD control × 100, where OD sample and OD control represent the optical density of the sample and control, respectively.

2.7.2 Fluorescence imaging of fungi. For bioimaging of fungi, 3.7 mg of SNN was dissolved in 100 μL of DMSO and diluted further to achieve a final concentration of 25 μM in a DMSO (0.01%) and DMEM (99.99%) solution. *C. albicans* (ATCC 24433) was cultured on Sabouraud Dextrose Agar (SDA). Edible bread was purchased and stored for one week, after which early-stage spores were collected. Two clean, grease-free glass slides were prepared, and a drop of saline was placed on each. Samples of *C. albicans*, *A. niger* (ATCC 16888), and early-stage fungal spores were carefully transferred onto the slides using a sterile teasing needle and evenly spread. To enhance the visualization of cell structures, a drop of SNN solution was applied as a stain to all slides. A coverslip was gently placed over each sample, ensuring no air bubbles were trapped. Excess stain was carefully blotted away using tissue paper. Finally, all slides were examined under a microscope (Olympus, Tokyo, Japan). Images of *C. albicans* and *A. niger* were obtained with a 20 μm scale bar, while fungi associated with bread spoilage were imaged with a 10 μm scale bar. The experiments were conducted with Institutional Ethics Committee (IEC) approval under IEC number IEC1: 515/2024.

2.7.3 H_2S-mediated fluorescence imaging of fungal species. About 3.7 mg of SNN was dissolved in 100 μL of DMSO and diluted further to obtain a final concentration of 25 μM in a DMSO (0.01%) and DMEM (99.99%) mixture. A drop of *C. albicans* and *A. niger* colonies was carefully transferred onto the slides, and a coverslip was gently placed on top of it. To culture bread molds, edible bread was stored at room temperature for one week to promote natural fungal growth. Both early-stage and mature fungal colonies were collected. Using a sterile teasing needle, the fungal material was gently transferred onto the prepared glass slides. For each fungal type, four experimental groups were prepared: (i) control

(untreated), (ii) 2-(aminooxy)acetic acid hydrochloride (AOAH; 1 mM) incubated for 2 h, (iii) SNN added, and (iv) AOAH (1 mM) incubated for 2 h and subsequently SNN was added. In AOAH-treated groups, the compound was added dropwise and incubated for 2 h. SNN was subsequently added dropwise, where applicable. The slides were observed under a fluorescence microscope at 40× magnification to assess fluorescence intensity and distribution across different treatment conditions. The data are expressed as mean ± SEM, with a sample size of n = 3. Statistical significance was evaluated using one-way ANOVA, and the analyses and graphs were generated using GraphPad Prism 8.0.1.

3. Results and discussion

3.1 Design of SNN

The design of SNN was based on the integration of a naphthalimide fluorophore with a nitro group as an H_2S-responsive unit and salicyl hydrazide as a versatile scaffold commonly employed in sensing applications. Naphthalimide derivatives represent a unique class of environmentally responsive fluorophores well-recognized for their strong fluorescence and high photostability, making them valuable tools in biological imaging,[29] anticancer therapeutics,[30] and photoinduced electron-transfer sensors.[31–36] Salicyl hydrazides, on the other hand, exhibit excellent optical properties due to their capacity for hydrogen bonding, excited-state intramolecular proton transfer (ESIPT), and intramolecular charge transfer (ICT), which enable photocontrollable color changes in both solution and solid states.[37] Despite their individual utility, the incorporation of a salicyl hydrazide moiety into a nitronaphthalimide framework has not been previously explored. Therefore, SNN was designed as a novel hybrid probe integrating two functional motifs to achieve dual functionality: selective H_2S detection and H_2S-mediated fluorescence imaging of fungi.

3.2 Structural characterization of SNN

The chemical structure of SNN was established by analyzing the FTIR, NMR, and mass spectral data. The IR spectrum displayed characteristic peaks for O–H, N–H, aromatic C–H, C═O, and C═C stretchings (Fig. S1). The ^{1}H NMR spectrum showed nine aromatic protons resonating between 7.011 and 8.821 ppm and the OH proton at 11.20 ppm (Fig. S2). The ^{13}C NMR spectrum confirmed the presence of nineteen carbons, supporting the structural framework of SNN (Fig. S3). The mass spectrum showed the molecular ion peak at 377 in accordance with the molecular weight of SNN and a base peak at 121 for the fragment ($C_7H_5O_2$) (Fig. S4a).

SNN: pale yellow; yield: 80% m.p: 300 °C; FTIR (cm^{-1}): 1737 (C═O str.), 3083 (Ar. C–H str.), 3284 (N–H str.), 3491 (O–H str.), ^{1}H NMR (400 MHz, ppm): δ 7.011–7.049 (t, J = 7.6 Hz, 1H), 7.062–7.083 (d, J = 8.4 Hz, 1H), 7.510–7.546 (t, J = 7.2 Hz, 1H), 7.977–7.996 (d, J = 7.6 Hz, 1H), 8.157–8.197 (t, J = 8 Hz, 1H), 8.611–8.631 (d, J = 8 Hz, 1H), 8.719–8.752 (m, 2H), 8.800–8.821 (d, J = 8.4 Hz, 1H), 11.175–11.326 (bs, OH); ^{13}C NMR (100 MHz): 115.71, 117.61, 120.23, 122.52, 123.45, 124.73, 126.36, 128.63, 130.15, 130.35, 130.76, 131.20, 133.25, 135.26, 150.23, 158.20, 161.05, 161.79, 166.58; MS (m/z) of $C_{19}H_{11}N_3O_6$: 377 (M), base peak at 121 ($C_7H_5O_2$).

3.3 Theoretical studies

Initially, the binding affinity of SNN for H_2S was assessed through computational studies, as presented in Fig. 1a. H_2S exhibited strong affinity for SNN, with a binding energy of 13.51 kJ mol^{-1}. The optimized structures of SNN and its reduced form are depicted in Fig. 1b and c. The frontier molecular orbital analysis of SNN revealed a distinct ICT character. In the ground state, the HOMO electron density was primarily localized on the salicyl moiety, while the LUMO was concentrated on the nitro-naphthalimide unit (Fig. 1d), consistent with the electron-withdrawing nature of the nitro group. A similar distribution was observed in the excited state, further supporting the occurrence of ICT. The calculated HOMO–LUMO energy gap decreased from 5.76 eV in the ground state to 5.06 eV in the excited state (Fig. 1e), indicating that lower energy is required for electronic excitation. This reduced gap implies enhanced electron delocalization and increased molecular polarizability, both of which can contribute to improved fluorescence efficiency and H_2S sensitivity.

As the H_2S-mediated reduction of the –NO_2 group is central to the sensing mechanism, the electronic structure of the reduced SNN was analyzed. The HOMO–LUMO distributions in both the ground and excited states (Fig. 1f and g) showed that the electron density remains localized around the amino-naphthalimide unit in both states, indicating minimal ICT. This stability is attributed to the electron-donating nature of the amino group. Notably, the HOMO–LUMO energy gap decreased from 5.78 eV in the ground state to 5.41 eV in the excited state, suggesting enhanced photophysical characteristics. The reduced energy gap may contribute to increased fluorescence quantum yields and a prolonged excited-state lifetime, thereby enhancing the brightness and sensitivity of SNN as a fluorescent probe. The ground-state (S_0) optimized geometries of SNN and its reduced form were calculated using the CAM-B3LYP/6-311G(d,p) level of theory with the SMD solvation model in water. The corresponding atomic coordinates are provided in Fig. S5a and S5b.

3.4 Electrochemical analysis of SNN

3.4.1 pH-dependent CV studies. CV of SNN was initially performed in the presence of Na_2S at pH 3. Two distinct reduction peaks appeared at −0.5 V and −0.7 V, accompanied by a single oxidation peak at −0.15 V under acidic conditions, as depicted in Fig. 2a. The increase in peak intensities with rising Na_2S concentrations is likely due to intermediate formation during the stepwise reduction of the nitro group in SNN. The first reduction peak at −0.5 V could correspond to the conversion of the nitro (–NO_2) group to the nitroso (–NO) group, while the second peak at −0.7 V could be attributed to the subsequent reduction to hydroxylamine (–NHOH). This sequential reduction is favored at pH 3 due to the high proton

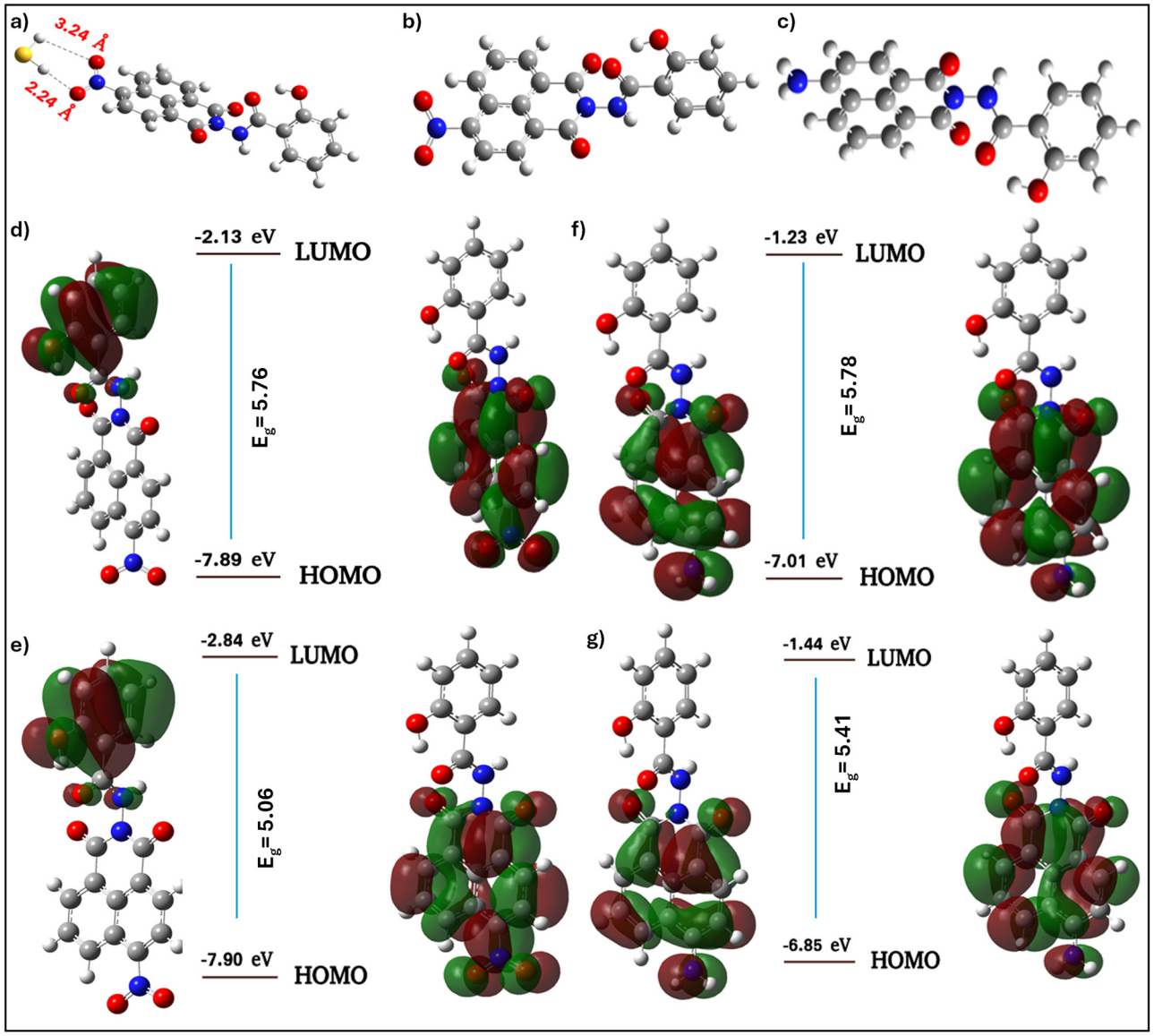

Fig. 1 (a) Interaction of SNN with H_2S. Ground-state optimized structures of (b) SNN and (c) reduced SNN. The HOMO and LUMO of SNN in (d) ground and (e) excited states. The HOMO and LUMO of reduced SNN in (f) ground and (g) excited states.

availability, which stabilizes the intermediates. However, complete reduction to the amine ($-NH_2$) group is less likely, as hydroxylamine remains relatively stable and resists further reduction in such an environment. Thus, the nitro–nitroso–hydroxylamine pathway predominates at lower pH, with full reduction to amine being thermodynamically less favorable. The oxidation peak might be due to sulfur oxidation. At acidic pH, hydrosulfide ions (HS^-) may be oxidized to elemental sulfur (S^0) or polysulfides (S_n^{2-}), contributing to the oxidation peak. Another notable observation during the analysis was that at pH 3, the initial colorless solution turned reddish-brown upon the addition of Na_2S, as depicted in the inset image of Fig. 2a.

At pH 7.4, the cyclic voltammograms exhibited two reduction peaks at −0.3 and −0.86 V, along with an oxidation peak at −0.1 V, as presented in Fig. 2b. Compared to acidic conditions, the lower availability of protons at pH 7.4 influences the reduction pathway of the $-NO_2$ group in SNN. The first reduction peak at −0.3 V shifted to −0.4 V upon an increase in concentration probably due to the partial reduction of $-NO_2$ to –NHOH, while the second peak at −0.86 V suggests the further reduction of –NHOH to $-NH_2$, which is more favorable under neutral conditions than at lower pH levels. The shift in the first reduction peak at −0.5 V at pH 3 to a less negative potential (−0.3 V) with an increase in pH to 7.4 indicates that protonation stabilizes the reduction process. Under neutral pH, sulfide from Na_2S predominantly exists as HS^- rather than H_2S, since the pK_a of H_2S is around 7. During the CV scan, HS^- undergoes oxidation at mild potentials, leading to the formation of S^0 or S_n^{2-}, which accounts for the oxidation

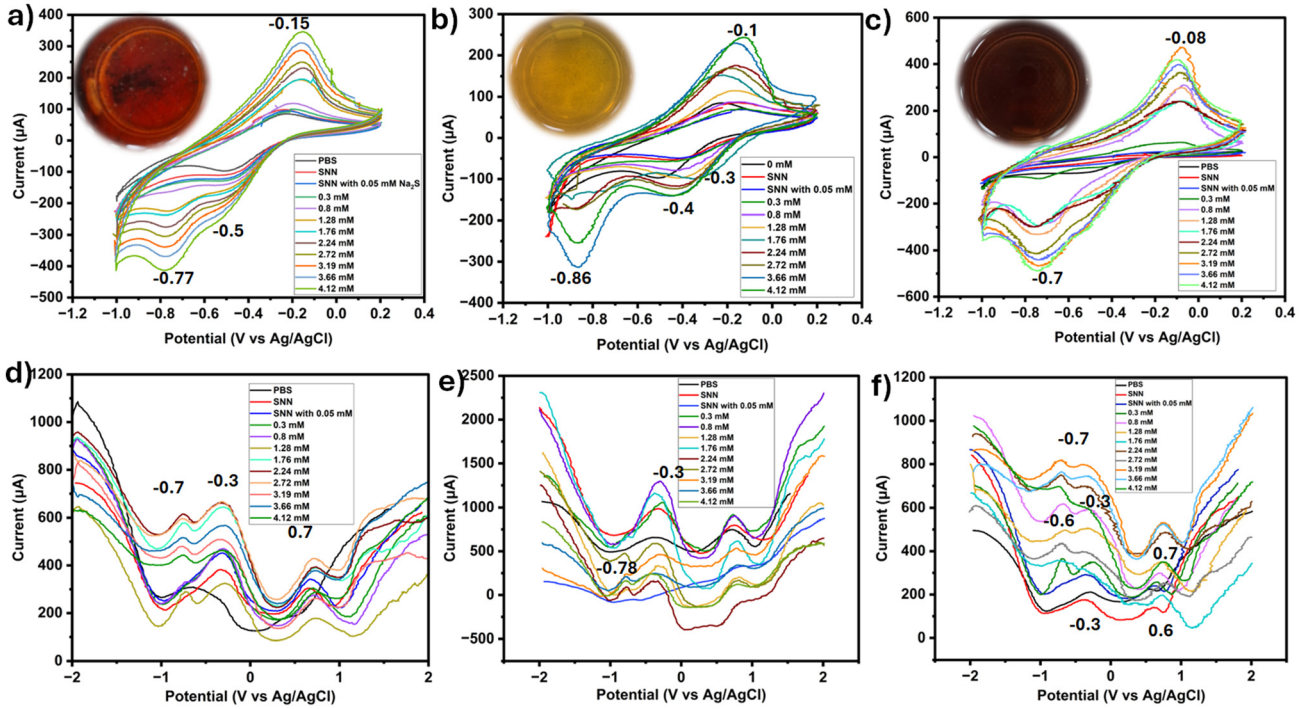

Fig. 2 Cyclic voltammograms at (a) pH 3, (b) pH 7.4 and (c) pH 9. Square wave voltammograms at (d) pH 3, (e) pH 7.4 and (f) pH 9.

peak at −0.1 V. This pH-dependent redox behavior suggests that neutral conditions promote deeper reduction of the nitro group while facilitating the oxidation of sulfide at lower potentials. Upon the addition of Na_2S at pH 7.4, the solution color changed to yellow as shown in the inset image of Fig. 2b.

At pH 9, the CV analysis showed a single reduction peak at −0.7 V and a single oxidation peak at −0.08 V, indicating a distinct redox behavior compared to that under lower pH conditions, as shown in Fig. 2c. In an alkaline environment, the availability of protons is significantly lower, which alters the reduction pathway of the $-NO_2$ group in SNN. Unlike at pH 3 and 7.4, where reduction occurs stepwise (nitro → nitroso → hydroxylamine → amine), the $-NO_2$ group undergoes direct reduction to $-NH_2$ at pH 9. The formation of intermediate species such as –NO or –NHOH is less favorable in the absence of sufficient protons. Instead, a two-electron reduction process occurs at −0.7 V, leading to the direct conversion of $-NO_2$ to $-NH_2$ in a single step. The peak at −0.08 V corresponds to the oxidation of sulfide (S^{2-}) to S^0 or S_n^{2-}. At pH 9, sulfide derived from Na_2S predominantly exists in the fully deprotonated S^{2-} form, in contrast to that at pH 7.4, where HS^- is the major species. The shift in the oxidation potential occurs because S^{2-} is a stronger reducing agent than HS^-, making its oxidation easier at a slightly lower potential. Overall, at pH 9, the redox behavior of SNN is strongly influenced by the reduced proton availability and the presence of a stronger reducing agent, resulting in a single-step nitro-to-amine reduction at −0.7 V, while the oxidation peak at −0.08 V reflects the conversion of sulfide species to sulfur compounds. At pH 9, the solution turned dark brown upon the addition of Na_2S (inset of Fig. 2c).

The pH-dependent color changes observed in the reaction mixture can be attributed to ICT behavior within the naphthalimide core, as shown in Fig. S6a. This ICT effect arises from a "push–pull" electronic system, where the electron-donating amino group (push) and the electron-withdrawing imide group (pull) create a delocalized π-system across the molecule. As depicted in the resonance structures, this delocalization can be modulated by pH-dependent ionization or electronic perturbation, leading to significant shifts in absorption and emission properties. Such behavior has been widely observed in 4-amino-1,8-naphthalimide derivatives, where solvent polarity and substituent effects influence their photophysical response.[38] The structural and electronic changes in SNN under different pH conditions, combined with redox interactions of sulfur species, contribute to the spectral (color) changes. Notably, all samples eventually turned yellow after 8 h (Fig. S6b–d), indicating the formation of a stable product, probably due to the completion of nitro group reduction. As the reaction reaches completion and the system stabilizes, further ICT-driven transformations are significantly minimized or cease altogether. The limit of detection (LOD: $3.3\sigma/S$ method) of SNN from CV measurements using a range of Na_2S concentrations (0–36.6 nM) was found to be 12.33 nM with an R^2 value of 0.9742 and a limit of quantification (LOQ: $10\sigma/S$ method) of 37.3 nM was obtained from the calibration curve, where σ is standard deviation = standard error × $\sqrt{n}$; n = 10 and S is the slope of the measurement curve, as shown in Fig. S7.

3.4.2 pH-dependent SWV studies. SWV plots at pH 3 initially showed peaks at −0.3 and 0.7 V. Upon the addition of

0.8 mM Na_2S, a new peak appeared at −0.7 V, indicating a specific interaction between SNN and S^{2-} ions, as shown in Fig. 2d. As the Na_2S concentration increased, the peak intensity continued to rise, reaching its maximum at 2.24 mM Na_2S. However, beyond this concentration, the intensity gradually decreased. At pH 3, the $-NO_2$ group in SNN undergoes a stepwise reduction, forming –NO and –NHOH intermediates. The emergence of the peak at −0.7 V following the addition of 0.8 mM Na_2S suggests that S^{2-} facilitated the further reduction of these intermediates, particularly the conversion of –NO to –NHOH. The maximum peak intensity observed at 2.24 mM Na_2S indicates that S^{2-} effectively enhanced electron transfer, thereby promoting the redox reaction. However, beyond this concentration, the decrease in peak intensity may be due to the limited availability of SNN molecules for further reduction, particularly for the final nitro-to-amine conversion, leading to a reduced current response. Consequently, the excess sulfur species present in the reaction medium may undergo reduction to S^{2-} and S^0.

At pH 7.4, before the addition of Na_2S, two peaks were initially observed at −0.3 and +0.7 V. However, as the Na_2S concentration increased to 1.76 mM, a new peak emerged at −0.78 V. This newly formed peak is likely associated with the reduction of the $-NO_2$ group to $-NH_2$, which becomes more favorable under physiological pH conditions. The appearance of the −0.78 V peak suggests that S^{2-} ions play a role in enhancing the complete reduction of $-NO_2$ to $-NH_2$ at this pH, as depicted in Fig. 2e. At pH 9, before the addition of Na_2S, two peaks were initially observed at −0.3 and 0.6 V, as shown in Fig. 2f. These peaks are likely attributed to redox-active functional groups within the SNN molecule. However, as the Na_2S concentration increased to 0.8 mM, distinct peaks emerged at −0.3, −0.6 and 0.7 V. The peak at −0.6 V is probably associated with the direct reduction of the $-NO_2$ group to $-NH_2$. With an increase in Na_2S concentration, the peak shifted to −0.7 V. This suggests that under alkaline conditions, S^{2-} ions enhance electron transfer, promoting a more efficient nitro reduction process. The peak at 0.7 V might be linked to the oxidation of sulfide species (S^{2-} or HS^-).

3.4.3 XPS analysis. XPS analysis of the electrolyte was conducted to examine the chemical changes in SNN and its interaction with Na_2S across the three pH levels studied. Survey spectra were acquired to assess the overall chemical composition and to observe the presence of carbon (C), nitrogen (N), oxygen (O), sulphur (S), and sodium (Na), as portrayed in Fig. 3a, f and k.

At pH 3, the C 1s spectrum exhibited peaks at 284.8, 285.2, 288.4, and 293.0 eV, corresponding to sp^2-hybridized carbon (C═C), C–N, C═O, and π–π* shake-up features from aromatic rings, respectively (Fig. 3b). The N 1s core-level spectrum was deconvoluted into peaks at 399.1, 400.0, and 401.1 eV, assigned to sp^2 nitrogen in the naphthalimide imide core (–N–CO), hydrazide (–NH–N═) bonds, and C–N–H, which could be due to $-NHOH/-NH_2$ groups (Fig. 3c). The O 1s spectrum showed peaks at 531.7 and 536.1 eV, attributed to carbonyl oxygen (C═O) and adsorbed water species, respectively

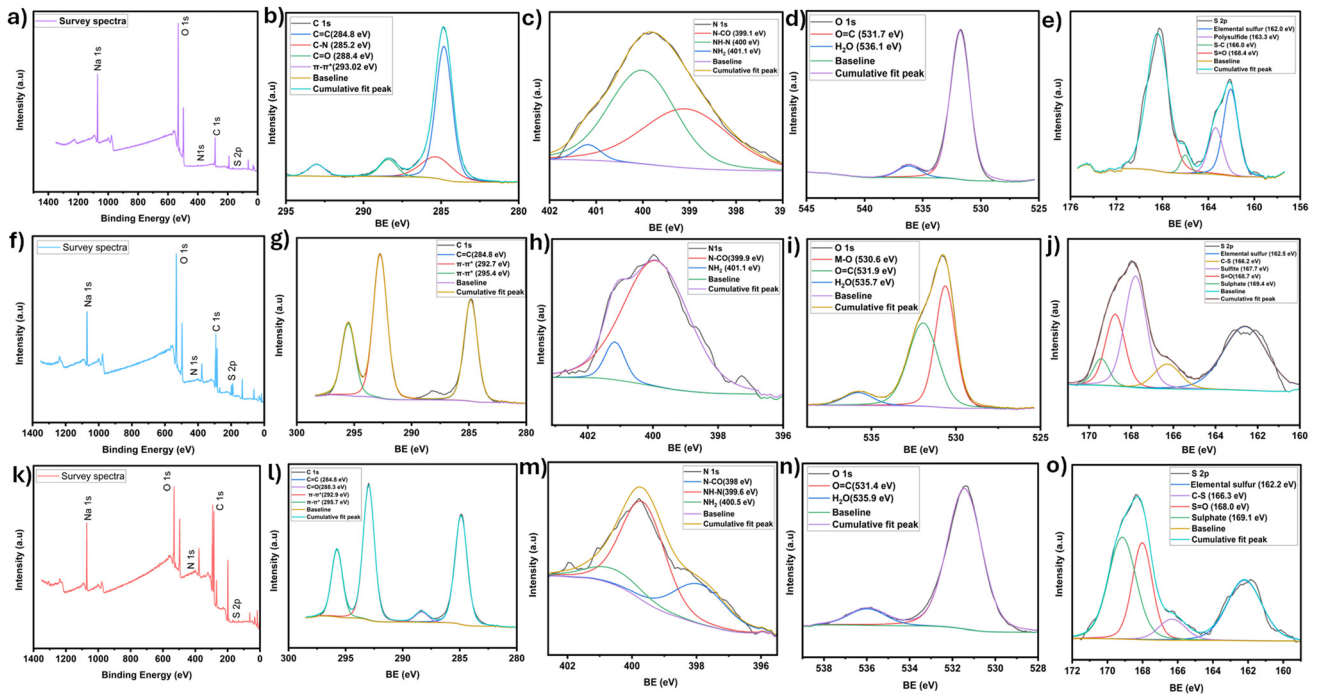

Fig. 3 (a) Survey spectra and deconvoluted spectra at pH 3 and the respective (b) C 1s, (c) N 1s, (d) O 1s and (e) S 2p spectra. (f) Survey spectra and deconvoluted spectra at pH 7.4 and the respective (g) C 1s, (h) N 1s, (i) O 1s and (j) S 2p spectra. (k) Survey spectra and deconvoluted spectra at pH 9 and the respective (l) C 1s, (m) N 1s, (n) O 1s and (o) S 2p spectra.

(Fig. 3d). Furthermore, the deconvoluted S 2p spectrum revealed peaks at 162.0 eV for S^0, 163.3 eV for S_n^{2-}, 166.0 eV for carbon-bonded sulfur (C–S), and 168.4 eV for sulfate (SO_4^{2-}) (Fig. 3e).

At pH 7.4, the C 1s spectrum exhibited peaks at 284.8, 292.7, and 295.4 eV, corresponding to sp^2-hybridized carbon (C═C) and π–π* shake-up features associated with aromatic rings (Fig. 3g). The N 1s spectrum displayed peaks at 399.9 eV, attributed to N–CO (imide nitrogen), and 401.1 eV, corresponding to the NH_2 group (Fig. 3h). In the O 1s spectrum, a peak at 530.6 eV was observed, which is characteristic of metal oxides, likely due to the formation of sodium oxides. Additionally, peaks at 531.9 and 535.7 eV were assigned to carbonyl oxygen (O═C) and adsorbed water (H_2O), respectively (Fig. 3i). The deconvolution of S 2p XPS spectra revealed multiple sulfur species, indicating a range of oxidation states. A peak at 162.5 eV corresponds to S^0, while that at 166.2 eV is attributed to the C–S bond. The presence of sulfite (SO_3^{2-}) is identified at 167.7 eV, whereas a distinct peak at 168.7 eV represents S═O bonding, possibly from sulfoxide or other partially oxidized sulfur species. Additionally, a peak at 169.4 eV is assigned to SO_4^{2-}, indicating the presence of fully oxidized sulfur. The combination of these peaks suggests a coexistence of both reduced and oxidized sulfur species, highlighting the complexity of sulfur chemistry in the system (Fig. 3j).

At pH 9, the C 1s spectrum exhibited peaks at 284.8 and 288.3 eV, corresponding to C═C and C═O, respectively (Fig. 3l). Additionally, SNN displayed π–π* shake-up satellite features at 292.9 and 295.7 eV, resulting from excitation between the filled and empty conjugated π states of the aromatic rings in the salicyl group and the naphthalimide moiety.[39] These higher binding energy peaks are intensified under basic pH due to enhanced conjugation following deprotonation of the –OH group in the salicyl moiety. The deconvoluted N 1s spectrum revealed peaks at 398, 399.6, and 400.5 eV, corresponding to sp^2 nitrogen in the naphthalimide imide core (–N–CO), hydrazide (–NH–N═) bonds, and C–N–H (amino groups), respectively (Fig. 3m). The O 1s spectrum showed peaks at 531.4 and 535.9 eV, assigned to carbonyl oxygen (C═O) and adsorbed water species, respectively (Fig. 3n). Additionally, the S 2p spectrum exhibited peaks at 162.2 eV for S^0, 166.3 eV for carbon-bonded sulfur (C–S), and in the range of 168.0 eV to 169.1 eV for sulfate species (Fig. 3o).

3.5 Absorbance studies

Absorbance spectra were recorded at pH 7.4, revealing a peak at 346 nm for SNN (100 μM). Upon the gradual addition of Na_2S (0.3–24.6 mM), the intensity of 346 nm peak decreased, while a new peak emerged at 460 nm, with an isosbestic point observed around 400 nm, indicating a clear transition between two species (Fig. 4a). Time-dependent studies were subsequently conducted, with spectra recorded every 3 min (Fig. 4b). The initial peak at 346 nm gradually decreased along with the progress in the intensity of the 460 nm peak. After 20 h, the spectrum showed only a single peak at 460 nm, confirming the completion of the reaction (Fig. 4b). This behavior is attributed to the H_2S-mediated reduction of the $–NO_2$ group of SNN to $–NH_2$. The electronic structure of SNN is altered due

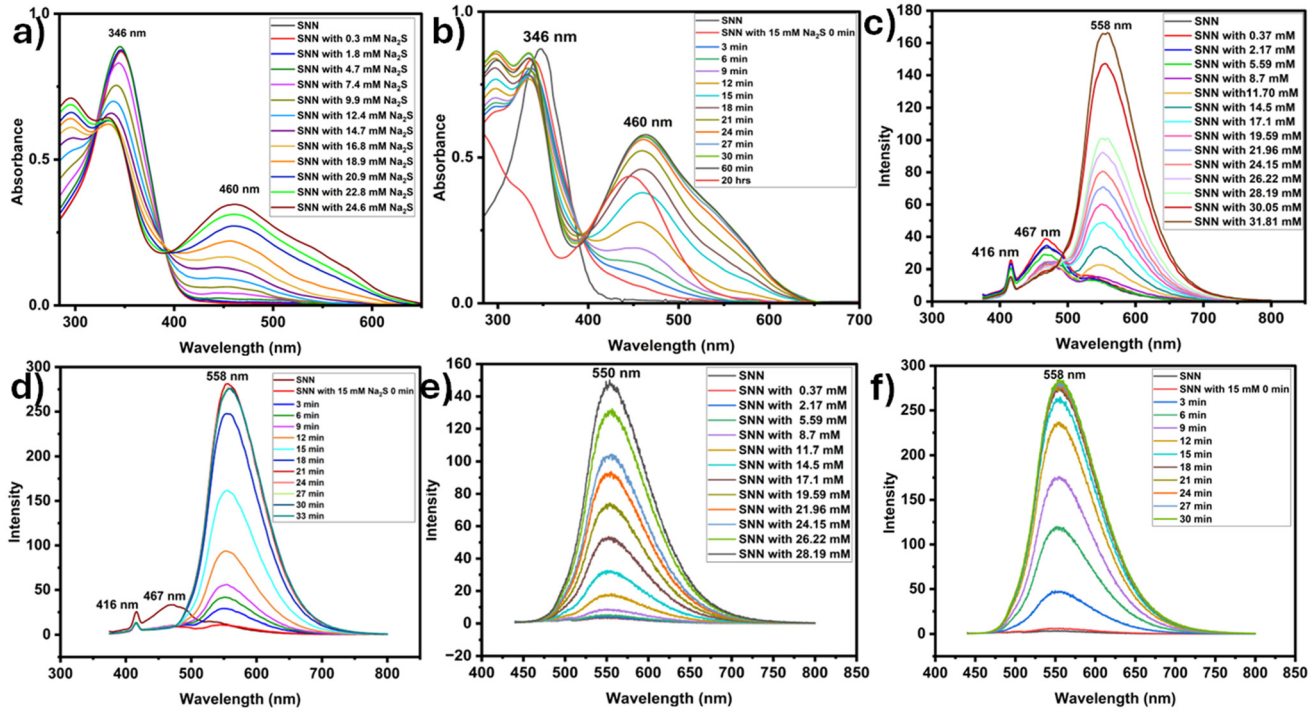

Fig. 4 UV Vis spectra of SNN: (a) concentration- and (b) time-dependent. Photoluminescence spectra of 100 μM SNN at λ_{ex} = 365 nm: (c) concentration- and (d) time-dependent. Photoluminescence spectra of 100 μM SNN at λ_{ex} = 430 nm: (e) concentration- and (f) time-dependent.

to the reduction of the $-NO_2$ group (electron-withdrawing) to the $-NH_2$ group (electron-donating), leading to a shift in absorbance. The emergence of the new peak at 460 nm reflects the distinct electronic transitions in the reduced product, and the disappearance of the original peak confirms the completion of the reaction. The isosbestic point indicates a clean, direct conversion without the accumulation of intermediates. The reduction is visually observable through the transition of a colorless solution before the addition of Na_2S to a brown colored reaction mixture with increasing concentration of Na_2S. The LOD ($3.3\sigma/S$ method) is found to be 13.20 mM with an R^2 value of 0.9557, and the LOQ ($10\sigma/S$ method) is 40.00 mM, where σ is the standard deviation = standard error × $\sqrt{n}$; n = 10 and S is the slope of the measurement curve, as shown in Fig. S8.

The color change observed at pH 7.4 in the UV studies (Fig. S9) prompted us to explore the H_2S detection capabilities of SNN colorimetrically at pH 7.4. The absorbance at 430 nm was recorded for the product formed after each incremental addition of Na_2S in colorimetric sensing experiments. This color change can be attributed to the conversion of the nitro group to an amino group. At pH 7.4, the interaction of Na_2S with the salicyl moiety likely leads to partial deprotonation, enhancing its nucleophilicity. This deprotonation may also contribute to the observed spectral changes. The LOD ($3.3\sigma/S$ method) of SNN at pH 7.4 from colorimetric measurements is found to be 2.73 mM with an R^2 value of 0.9982 and an LOQ ($10\sigma/S$ method) of 8.27 mM was obtained from the calibration curve shown in Fig. S10, where σ is the standard deviation = standard error × $\sqrt{n}$; n = 9 and S is the slope of the measurement curve.

3.6 Emission studies

3.6.1 Emission studies of SNN at pH 7.4. The Na_2S-responsive fluorescence properties of SNN (100 μM) were further investigated. The 3D emission spectrum recorded for SNN at physiological pH displayed maximum excitation at 365 nm, as shown in Fig. S11. Neat SNN showed weak emissions at 416 and 467 nm. Upon incremental addition of Na_2S from 0.37 to 31.8 mM, the peak at 467 nm decreased, and a new peak at 558 nm emerged with increasing intensity, as shown in Fig. 4c. Time-dependent emission behavior of SNN (100 μM) was examined by adding 17 mM Na_2S and recording spectra every 3 min, as depicted in Fig. 4d. Neat SNN showed a peak at 467 nm, which underwent a drastic reduction in intensity after 3 min. The peak at 558 nm exhibited a rise in intensity every 3 min, and by 30 min, an intense peak was observed. The ratiometric behavior of the emission profile upon Na_2S addition arises because the reduction of the nitro group changes the conjugation and electronic density in the molecule. As Na_2S is added incrementally, the peak at 467 nm decreases (associated with the nitro form), while the peak at 558 nm increases (associated with the amino form). The fluorescence observed under 365 nm illumination is depicted in Fig. S12. Moreover, SNN displays good selectivity towards Na_2S compared to other biological sulfur-containing analytes such as Cys, GSH and biologically relevant metal salts like $ZnCl_2$, $MgSO_4$, $CaCl_2$, $AlCl_3$, $CuCl_2$, $FeCl_3$, and $HgCl_2$ (Fig. S13).

3.6.2 Confirmation of H_2S-mediated reduction of SNN. The 3D spectrum of SNN (100 μM) was recorded after 1 h of Na_2S addition (31.8 mM), which exhibited a marked shift in excitation wavelength from 365 nm to 430 nm and a prominent emission at around 550 nm, as portrayed in Fig. S14. This proves the proposed nitro-to-amino reduction upon Na_2S addition. Concentration- and time-dependent spectra were recorded at an excitation wavelength of 430 nm, as shown in Fig. 4e and f. The ratiometric response in fluorescence behavior observed at λ_{ex} = 365 nm was absent at λ_{ex} = 430 nm. Instead, a turn-on fluorescence response, which intensifies with increasing Na_2S concentration, is observed. A similar trend is observed in the time-dependent experiments, wherein the intensity of the peak at 550 nm increased with time. This indicates that the reduction reaction continues to proceed within the timeframe of the study, leading to a greater population of the amino form and a corresponding increase in emission intensity. At λ_{ex} = 430 nm, only the amino form of the molecule is selectively excited, and the resulting emission peak at 550 nm corresponds to the fluorescence of this reduced species. The absence of ratiometric behavior suggests that the system is dominated by the amino form, which displays a "turn-on" response as its concentration increases. The fluorescence observed under 430 nm illumination is depicted in Fig. S15. The LOD of SNN from fluorescence measurements at pH 7.4 (λ_{ex} = 365 nm) is 10.83 mM with an R^2 value of 0.977 and an LOQ of 32.84 mM, where σ is the standard deviation = standard error × $\sqrt{n}$; n = 10 and S is the slope of the measurement curve, as shown in Fig. S16.

The fluorescence lifetime studies provide information about the time a fluorophore takes to transit from its excited state to ground state, following the absorption of a photon and subsequent fluorescence emission. The lifetime measurements of pure SNN (100 μM) and in the presence of 15 mM Na_2S were investigated and are presented pictorially in Fig. S17. Decay plots are best fitted with bi-exponential fitting, and the lifetime values are summarized in Table S1. SNN is dominated by a long-lived component (2.02 ns, 83%) with a minor slower decay component (4.63 ns, 17%). However, the lifetimes are significantly shortened (τ_1 = 1.80 ns, 30.44%, and τ_2 = 2.21 ns, 69.5%) in SNN treated with Na_2S. This significant shortening of fluorescence lifetimes is due to the structural transformation from a nitro to an amino group as observed in the theoretical studies, which modifies the electronic structure and promotes faster non-radiative decay pathways. This behavior is consistent with the observed changes in the fluorescence emission and further supports the reduction of SNN by Na_2S.

Finally, to confirm the H_2S-mediated nitro to amino group reduction in SNN, mass spectrometric analysis of SNN was performed. The spectrum (Fig. S4b) recorded after 24 h of addition of 17.1 mM Na_2S showed an M + 1 peak at m/z = 348.24, consistent with its molecular weight ($C_{19}H_{13}N_3O_4$: 347).

3.6.3 Emission studies of SNN at pH 3 and 9. Although the primary focus is to study the fluorescence behavior of SNN at physiological pH, we also examined its response under acidic

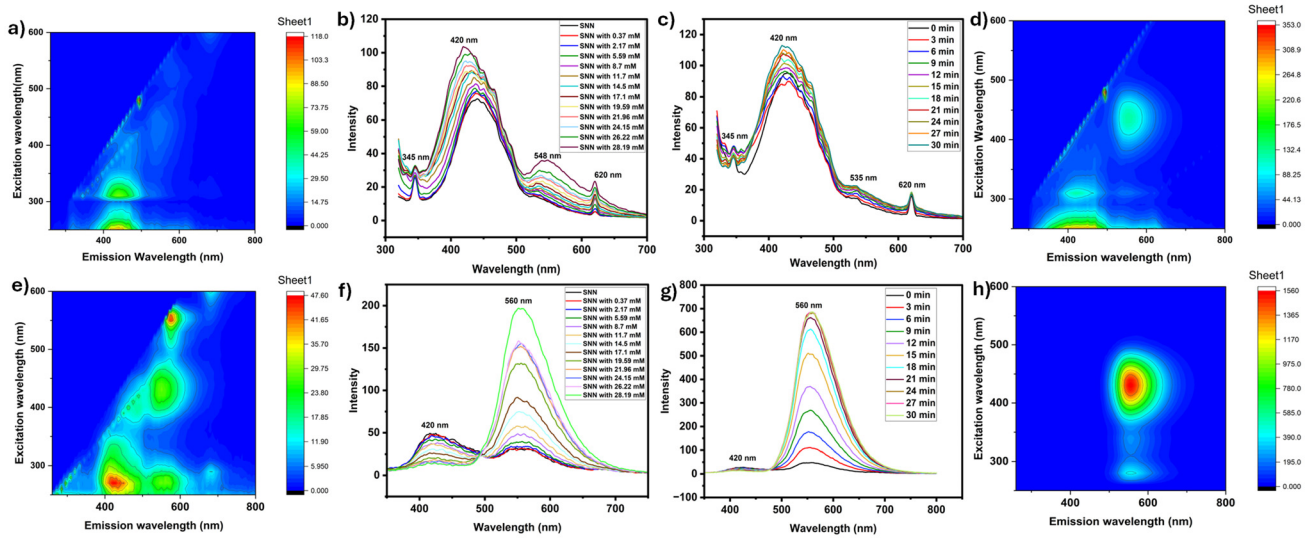

Fig. 5 Photoluminescence spectra of 100 μM SNN at pH 3 at λ_{ex} = 310 nm: (a) 3D spectrum, (b) concentration-dependent 2D spectra, (c) time-dependent 2D spectra, and (d) 3D spectrum after addition of 17.1 mM Na_2S. Photoluminescence spectra of 100 μM SNN at pH 9 at λ_{ex} = 270 nm: (e) 3D spectrum, (f) concentration-dependent 2D spectra, (g) time-dependent 2D spectra, and (h) 3D spectrum after addition of 17.1 mM Na_2S.

(pH 3) and basic (pH 9) conditions. The 3D fluorescence spectrum of 100 μM SNN at pH 3 revealed a maximum excitation at 310 nm (Fig. 5a). A concentration-dependent study using Na_2S (0–28.19 mM) showed a progressive increase in fluorescence intensity, with a prominent emission peak at 420 nm. Notably, with increasing Na_2S concentration, a new emission peak emerged at 548 nm, which intensified with higher Na_2S concentrations. The 420 nm peak is likely attributed to SNN, while the 548 nm peak may correspond to its reduced form, where the nitro group has been converted to an amino group. The minor peaks, particularly at 345 nm and 620 nm, could be associated with intermediate species formed during the reduction process under acidic conditions, wherein incomplete or stepwise reduction pathways might occur (Fig. 5b). Time-dependent fluorescence studies were performed using 100 μM SNN and 17.1 mM Na_2S, with spectra recorded at 3 min intervals. The emission profile closely resembled that of the concentration-dependent study, although only a weak peak appeared at 535 nm. This suggests that the reduction of the nitro group to the amino form proceeds much more slowly at acidic pH compared to that at physiological pH. The reduced reaction rate under acidic conditions may be due to the limited availability of reactive HS^- species, slower electron transfer kinetics, or decreased stability of intermediates necessary for the conversion (Fig. 5c). Following the time-dependent experiment, a 3D fluorescence spectrum was recorded to assess changes in the emission profile. Unlike the 3D spectrum at pH 7.4 after Na_2S addition, which showed the characteristic emission of the reduced form, the spectrum at pH 3 revealed distinct excitation peaks at 310 nm and 430 nm. This indicates that the nitro group remained partially unreduced, and complete conversion to the amino form did not occur under acidic conditions. These findings highlight the slower and incomplete reduction of SNN at lower pH values (Fig. 5d).

The 3D fluorescence spectrum of 100 μM SNN at pH 9 exhibited a maximum excitation at 270 nm (Fig. 5e). In the concentration-dependent study with Na_2S (0–28.19 mM), a clear ratiometric fluorescence response was observed: the emission intensity at 420 nm gradually decreased, while a new peak at 560 nm increased with rising Na_2S concentrations. Compared to pH 3 and pH 7.4, SNN displayed significantly higher fluorescence intensity at pH 9, indicating enhanced probe responsiveness under basic conditions (Fig. 5f). Time-dependent studies using 17.1 mM Na_2S further supported this observation. Fluorescence spectra recorded at 3 min intervals revealed that within the initial 0–3 min, the 420 nm peak corresponding to SNN had completely disappeared, while the 560 nm peak, which is indicative of the amino-reduced form, showed strong intensity. This rapid and complete shift suggests that the nitro-to-amino conversion proceeds most efficiently under basic conditions (Fig. 5g). The post-reduction 3D spectrum revealed a single dominant excitation at 430 nm, similar to that observed at pH 7.4, confirming complete conversion of the nitro group to the amino form. This high reactivity at pH 9 is likely due to the increased availability of the nucleophilic HS^- species, which facilitates faster and more efficient reduction (Fig. 5h).

3.7 Fluorescence imaging studies

3.7.1 Cytotoxicity and photostability assessment of SNN. Assessing the cytotoxicity of SNN is a crucial step for biological imaging, especially in live-cell or *in vivo* applications. Therefore, to evaluate the biocompatibility of SNN, its cytotoxicity was assessed in HEK293T cells using the MTT assay over a concentration range of 5–25 μM. A dose-dependent decrease in cell viability was observed: 93% viability at 5 μM and 65% at 25 μM (Fig. S18a). These results support the suitability of SNN for biological imaging applications.

The photostability of a fluorophore is a critical factor in fluorescence imaging, as prolonged exposure to excitation light can lead to signal degradation. Therefore, the fluorescence response of SNN was assessed by exposing it to 20 W UV light for various durations. Interestingly, the photoluminescence spectra of SNN (λ_{ex} = 350 nm) recorded after 1, 3, and 5 h of UV light exposure (Fig. S18b) showed no noticeable changes in either fluorescence intensity or shift in the emission peak, confirming its excellent resistance to photobleaching under prolonged UV exposure.

3.7.2 Fluorescence imaging of *C. albicans*. Wet mount preparations of *C. albicans* stained with SNN, without any incubation period, produced clear, high-contrast fluorescence images, enabling detailed morphological visualization (Fig. 6b and c). Remarkably, the fluorophore exhibited prominent nuclear localization, as shown in Fig. 6d, suggesting a specific interaction of SNN with nuclear components. Although identifying the exact molecular target is beyond the scope of this study, the observed nuclear targeting highlights the potential of SNN for real-time fungal diagnostics. The strong fluorescence observed in *C. albicans* may be due to the reduction of the nitro group to an amino group in SNN, likely mediated by endogenous H_2S present in the fungi, as previously reported by Yan *et al.*[4] In contrast, the control cells exhibited green fluorescence (Fig. 6a), likely due to autofluorescence from *C. albicans*; however, no distinct nuclear localization was observed, highlighting a clear difference from the SNN-stained cells.

3.7.3 Fluorescence imaging of *A. niger*. Wet mount preparations of *A. niger* stained with SNN exhibited minimal fluorescence (Fig. 6f and g) compared to unstained cells (Fig. 6e), suggesting that the probe may not have effectively permeated the hyphal cell membrane, resulting in weak or negligible staining.

3.7.4 Real-time fluorescence imaging of fungi in spoiled bread. A powdery white fungal growth from stored edible bread was collected and examined using SNN under a fluorescence microscope. Wet mount imaging after SNN staining without any subsequent incubation period revealed budding cells and fungal colonies with exceptional contrast, as portrayed in Fig. 6i–k, while the untreated cells did not show any fluorescence (Fig. 6h). Interestingly, unlike in *C. albicans*, the fluorophore exhibited a uniform distribution across the entire cell without any evident nuclear localization. This broader uptake indicates effective binding of SNN to general fungal components, making it an effective tool for detecting environmental fungal contamination in food.

3.7.5 Fluorescence imaging of fungal H_2S production mediated by enzymatic activity. Absorbance, electrochemical, and fluorescence studies confirmed the potential of SNN as an H_2S sensor *via* nitro group reduction, which generates corresponding detectable signals. While colorimetric and electrochemical approaches are effective for bulk quantification in solutions or on electrode surfaces, they lack the spatial resolution and real-time imaging capability required to visualize H_2S dynamics within fungal cells. Fluorescence-based measurements have added advantages, including high sensitivity and resolution, live-cell compatibility, specific localization, and capability, for real-time dynamic studies for fungal imaging.[40]

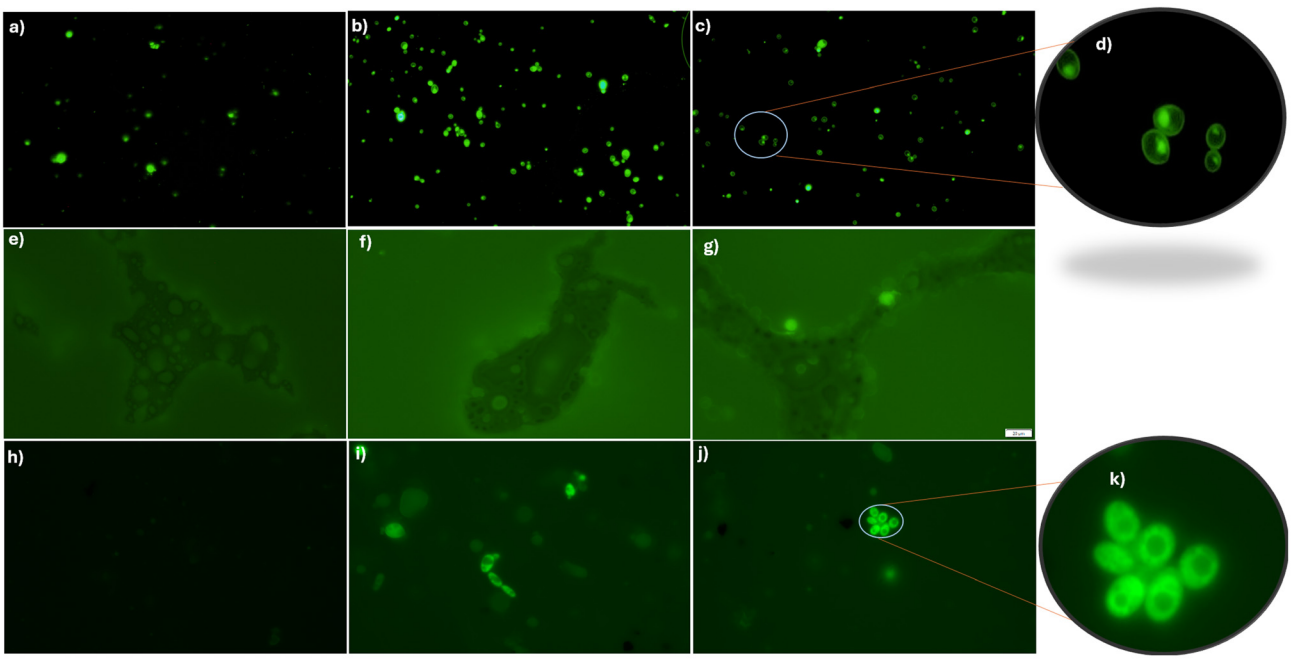

Fig. 6 Fluorescence imaging of *C. albicans*: (a) control, (b and c) SNN stained cells, and (d) enlarged image of SNN stained cells. Fluorescence imaging of *A. niger*: (e) control and (f and g) SNN stained cells. Fluorescence imaging of bread mold: (h) control, (i and j) SNN stained cells, and (k) enlarged image of SNN stained cells.

Despite considerable progress in the development of H_2S probes, their application in microorganisms, especially for detecting and studying fungi, remains largely underexplored. Several fungi are known to produce endogenous H_2S as part of their normal metabolism, particularly *via* the cysteine degradation pathway driven by CBS, cystathionine γ-lyase or cysteine desulfhydrase, akin to that in other eukaryotes and sulfur assimilation processes. Hence, in the present study, the ability of SNN is further explored as a selective fluorescent probe for H_2S-mediated imaging of fungi, which is of great importance and urgently desirable to better understand the detailed physiological and pathological effects of H_2S in microbes. The role of endogenous H_2S in our imaging assays was assessed in the presence of AOAH, a selective CBS inhibitor of H_2S biosynthesis, as detailed in section 2.7.3. Fungal imaging was performed on *C. albicans*, *A. niger*, and bread mold, with careful examination of both bud and hyphal morphologies.

C. albicans is a pathogenic yeast and a model organism for fungal pathogenesis. This opportunistic fungal pathogen is known to produce H_2S through cysteine desulfhydrase activity.[41,42] H_2S promotes the formation of biofilms, which is a major virulence factor that facilitates surface colonization and increases resistance to antifungal agents.[43] H_2S contributes significantly to the survival and pathogenicity of *C. albicans* by maintaining redox balance and mitigating oxidative stress through the scavenging of reactive oxygen species (ROS), which enhances the resilience of the fungus against host immune defenses.[8] Furthermore, H_2S helps the fungus to adapt to dynamic host environments and strengthens fungal tolerance to various environmental stresses, including oxidative, nitrosative, and thermal challenges. Emerging studies indicate that endogenous H_2S influences the expression of virulence-associated genes and regulates the yeast-to-hyphae transition, a key feature of pathogenicity.[44,45] Effective imaging of *C. albicans* is thus essential for obtaining deeper insights into its biofilm development and host–pathogen interactions. In *C. albicans*, neither the control (Fig. 7a) nor the cells treated with AOAH alone displayed any detectable fluorescence (Fig. 7b). Interestingly, intense fluorescence was detected for cells after staining with SNN alone, which indicated the abundant generation of endogenous H_2S in *C. albicans* (Fig. 7d). However, upon 2 h incubation with AOAH and further staining with SNN, fluorescence intensity was reduced, which validated the specific detection of endogenous H_2S by SNN (Fig. 7c). These imaging results confirm the presence of endogenous H_2S in *C. albicans*, as previously reported by Yan *et al.*[4] The marked reduction in fluorescence following AOAH treatment validates the specificity of SNN for intracellular H_2S. The com-

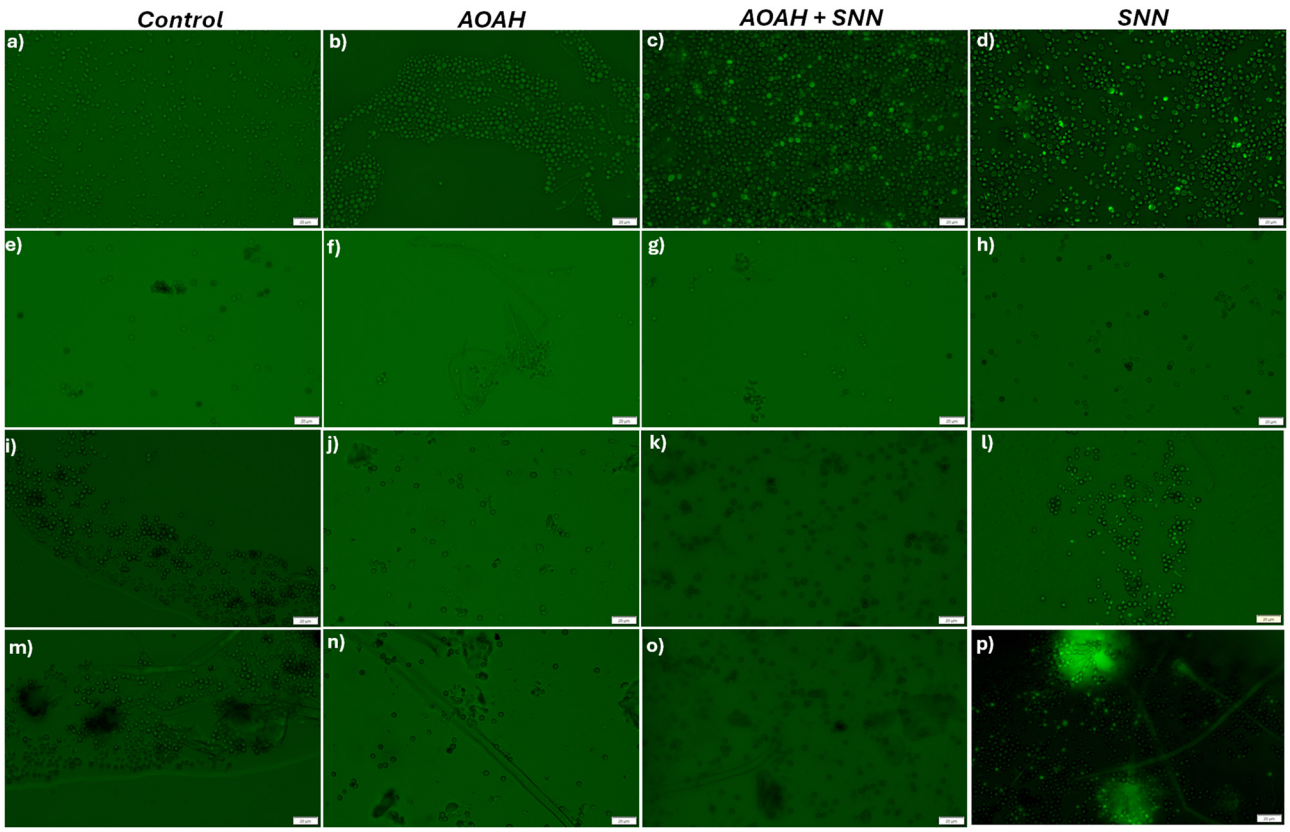

Fig. 7 Fluorescence imaging of *C. albicans*: (a) control, (b) AOAH, (c) AOAH and SNN stained cells and (d) SNN stained cells. Fluorescence imaging of *A. niger*: (e) control, (f) AOAH, (g) AOAH and SNN stained cells and (h) SNN stained cells. Fluorescence imaging of buds in bread mold: (i) control, (j) AOAH, (k) AOAH and SNN stained cells and (l) SNN stained cells. Fluorescence imaging of hyphae in bread mold: (m) control, (n) AOAH, (o) AOAH and SNN stained cells and (p) SNN stained cells.

parison of fluorescence intensity from all the studied groups is portrayed in Fig. 8.

The role of H_2S in *A. niger*, a filamentous fungus widely used in industrial applications and known as an opportunistic pathogen, is not as extensively studied as in *C. albicans*. It can produce H_2S through cysteine and methionine metabolism under sulfur-limited or reductive growth conditions. There is a need for targeted studies to elucidate the mechanisms of H_2S production and its physiological roles in *A. niger*, particularly regarding its stress responses. The control (Fig. 7e), and cells incubated with AOAH (Fig. 7f), stained with SNN after AOAH incubation (Fig. 7g) and stained with SNN (Fig. 7h) did not display any fluorescence. The endogenous H_2S levels in *A. niger* were too low to detect. Although Guo *et al.* demonstrated that the CBS gene in *A. niger* mediates conversion of cysteine to H_2S,[46] our results imply that either the steady-state H_2S levels in *A. niger* are below the detection threshold of SNN or that SNN is unable to efficiently penetrate the thick cell wall to access intracellular H_2S. Additionally, the distinct structural morphology of *A. niger*, particularly the presence of melanin in its cell walls, may play a role. Melanin is known to act as a physiological redox buffer, providing structural rigidity and protection against antimicrobial agents, and has been described as a "fungal armour" that enhances fungal survival under harsh conditions and contributes to virulence in several species.[47,48] We hypothesize that the absence of a detectable signal in *A. niger* is likely attributable to intrinsically low H_2S output and/or limited probe penetration through the thick fungal cell wall. However, direct uptake studies and quantitative measurements of intracellular H_2S would be required to validate this.

These species-specific differences likely reflect their ecological and pathogenic strategies. In *C. albicans*, H_2S production is closely linked to virulence, supporting oxidative stress resistance, redox homeostasis, protein sulfhydration, and hyphal development, whereas in *A. niger*, H_2S arises primarily as a byproduct of sulfur assimilation and is not associated with pathogenicity or adaptive stress responses. Consequently, *A. niger* generates significantly less free H_2S than *C. albicans* under both basal and induced conditions, explaining the absence of SNN fluorescence in this saprophytic organism.

3.7.6 Fluorescence imaging of non-enzymatic H_2S production in bread spoilage fungi. H_2S may also be released non-enzymatically under certain environmental conditions,

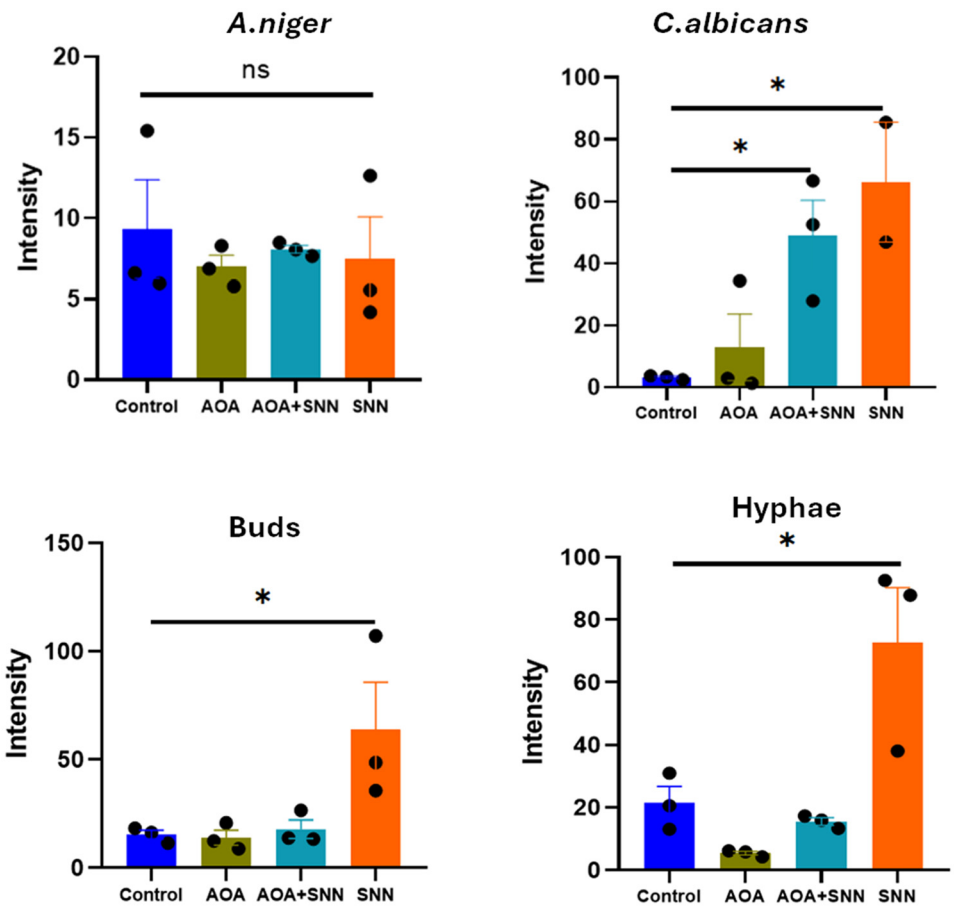

Fig. 8 Comparative bar chart illustrating the fluorescence intensity of control, AOAH (marked as AOA)-treated, AOAH with SNN, and SNN-stained samples for *C. albicans*, *A. niger* and bread mold (both buds and hyphae). Data are presented as mean ± SEM from $n = 3$ independent experiments. Statistical significance was determined using one-way ANOVA (GraphPad Prism 8.0.1); $p < 0.05$ was considered significant.

especially during the degradation of sulfur-containing amino acids in spoiled food or bread. The role of H_2S in bread spoilage fungi is not yet well-documented in the literature but based on fungal physiology and H_2S functions in other microorganisms, several potential roles of H_2S have been identified, including antioxidant and stress protection, hyphal development, biofilm formation, and virulence gene expression in fungi commonly associated with bread spoilage, such as *Aspergillus, Penicillium*, *Rhizopus*, *Mucor and Cladosporium* species. Spoilage fungi may similarly use H_2S to regulate spore germination, hyphal growth, or morphological adaptation to food substrates like bread. Therefore, fluorescent H_2S probes may offer promising approaches for studying endogenous H_2S *in situ*.

Fluorescence imaging was conducted on stored bread samples as described in section 2.7.3, targeting both budding and hyphal forms to evaluate morphological differences and the corresponding fluorescence behavior. In both forms, no detectable fluorescence was observed in the control (Fig. 7i and m), AOAH-incubated cells (Fig. 7j and n), or AOAH-incubated and subsequently SNN-stained cells (Fig. 7k and o). In contrast, strong fluorescence was detected in both buds and hyphae treated with SNN alone (Fig. 7l and p), suggesting the presence of endogenous H_2S. This observation is consistent with the established fungal physiology. For instance, *C. albicans* is known to produce considerable levels of endogenous H_2S, particularly under stress conditions, as part of its redox balance and virulence strategies. Likewise, bread molds such as *Penicillium* and *Rhizopus* possess active sulfate assimilation and transsulfuration pathways, enabling sulfur metabolism and the potential generation of H_2S as a metabolic byproduct.

However, while the observed fluorescence in bread mold stained with SNN suggests endogenous H_2S production, there is currently no direct experimental evidence or quantification confirming this. Given that bread molds likely possess the metabolic capability to generate H_2S, the strong fluorescence observed in SNN-treated samples supports this hypothesis. Nonetheless, direct experimental validation is needed to confirm whether bread mold species indeed produce detectable levels of endogenous H_2S and to identify the precise physiological or environmental conditions under which this occurs.

4. Comparison of SNN with the reported 2,4-dinitrophenyl-based probes

In comparison with the recently reported 2,4-dinitrophenyl-based probe by Yan *et al.*,[4] which demonstrated robust H_2S detection and imaging in oral fungi in microscopy, flow cytometry, and colony assays, SNN presents distinct structural and functional advantages. The reported probe is built on a 2,4-dinitrophenyl scaffold and operates through H_2S-triggered thiolysis of the dinitrophenyl ether, whereas SNN possesses a nitronaphthalimide core and functions *via* H_2S-mediated nitro reduction. The reported probe exhibits turn-on fluorescence enhancement at 620 nm, while SNN displays ratiometric behavior under 365 nm excitation and turn-on fluorescence under 430 nm excitation. Functionally, the reported probe emphasizes systematic quantification of H_2S and multimodal validation in pathogenic oral fungi, whereas SNN enables rapid wet-mount visualization of *C. albicans* with minimal sample preparation steps and provides high-contrast nuclear fluorescence. Both probes exhibit excellent selectivity towards H_2S, yet they cater to different application niches: the reported probe is optimized for comprehensive quantitative analysis, while SNN offers rapid response, species-selective imaging, and broad applicability against both pathogenic and spoilage fungi. Moreover, SNN exhibits dual functionality, enabling both optical and electrochemical detection of H_2S over a wide pH range. Collectively, these studies expand the toolkit for fungal H_2S research and highlight opportunities for cross-validation and comparative studies in future investigations.

5. Conclusion and future scope

A new fluorescent probe, SNN, was successfully developed for the selective detection of H_2S by integrating both optical and electrochemical sensing modalities for real-time imaging of fungi. Complementary theoretical and electrochemical analyses elucidated the stepwise reduction of the nitro group in SNN and confirmed an ICT-based detection mechanism, with electrochemical measurements demonstrating nanomolar-level sensitivity. The probe enabled high-contrast, wet-mount imaging of *C. albicans* with selective nuclear localization, while also visualizing spoilage-associated fungi with distinct cytoplasmic staining. The H_2S-triggered fluorescence was validated through inhibition studies using 2-(aminooxy)acetic acid hemihydrochloride, confirming endogenous H_2S as the activation source. The ability of SNN to differentiate fungal species and localize in intracellular targets underscores its potential as a versatile tool for microbial diagnostics, antifungal research, and food safety monitoring. Future studies should explore the molecular basis of its selective localization and expand its application to a broader range of fungal pathogens.

Author contributions

Ranjana M. performed the synthesis, structural, optical, and electrochemical characterization, preparation of fluorescent stain, data analysis, and drafted the original manuscript. Namita N. Kashyap performed MTT assay and fluorescence imaging of HEK293T cells. Dinesh Upadhya supervised biological studies. Anshuman Bera conducted computational studies. Sivaranjana Reddy Vennapusa supervised the computational studies. Prakash Peralam Yegneswaran provided fungal cultures and revised the original manuscript. Prajoy

Kumar Mitra assisted in conducting fluorescence lifetime measurement experiments. Sudhakar Y. N. supervised the electrochemical studies and revised the original manuscript. Suresh D. Kulkarni provided spectrofluorometer instrument facilities. Dhanya Sunil planned the research hypothesis, supervised the experiments, and revised the original manuscript.

Conflicts of interest

Indian patents (Application No. 202441103743) have been filed for this study. The authors declare that they have no known competing interest.

Data availability

The data supporting this article have been included as part of the supplementary information (SI). See DOI: https://doi.org/10.1039/d5an00783f.

Any other data reported in this manuscript are available on request.

Acknowledgements

During the manuscript preparation, the authors used Grammarly and ChatGPT for language editing. After using this tool/service, the author(s) reviewed and edited the content as needed and take(s) full responsibility for the content of the publication.

References

1 M. C. Fisher, N. J. Hawkins, D. Sanglard and S. J. Gurr, Worldwide emergence of resistance to antifungal drugs challenges human health and food security, *Science*, 2018, **360**(6390), 739–742, DOI: 10.1126/science.aap7999.

2 C. Munteanu, D. Munteanu and G. Onose, Hydrogen sulfide (H_2S)–Therapeutic relevance in rehabilitation and balneotherapy: Systematic literature review and meta-analysis based on the PRISMA paradigm, *Balneo. PRM Res. J.*, 2021, **12**(3), 176–195.

3 S. Panthi, H. J. Chung, J. Jung and N. Y. Jeong, Physiological importance of hydrogen sulfide: Emerging potent neuroprotector and neuromodulator, *Oxid. Med. Cell. Longevity*, 2016, **2016**, 9049782, DOI: 10.1155/2016/9049782.

4 Q. Yan, S. He, L. Feng, M. Zhang, C. Han, Y. Wu, *et al.*, A turn-on fluorescent probe for highly selective detection and visualization of hydrogen sulfide in fungi, *Molecules*, 2024, **29**(3), 577, DOI: 10.3390/molecules29030577.

5 J. Yang, P. Minkler, D. Grove, R. Wang, B. Willard, R. Dweik, *et al.*, Non-enzymatic hydrogen sulfide production from cysteine in blood is catalyzed by iron and vitamin B6, *Commun. Biol.*, 2019, **2**, 194, DOI: 10.1038/s42003-019-0431-5.

6 A. Krejčí, Z. Palková and Ľ. Tomáška, Alternative sulphur metabolism in the fungal pathogen Candida parapsilosis, *Nat. Commun.*, 2024, **15**, 53442, DOI: 10.1038/s41467-024-53442-8.

7 R. Wang, Hydrogen sulfide: The third gasotransmitter in biology and medicine, *Antioxid. Redox Signaling*, 2010, **12**(9), 1061–1064, DOI: 10.1089/ars.2009.2938.

8 W. Chang, M. Zhang, X. Jin, H. Zhang, H. Zheng, S. Zheng, *et al.*, Inhibition of fungal pathogenicity by targeting the H_2S-synthesizing enzyme cystathionine β-synthase, *Sci Adv.*, 2022, **8**(52), eadd5366, DOI: 10.1126/sciadv.add5366.

9 K. Shatalin, E. Shatalina, A. Mironov and E. Nudler, H_2S: A universal defense against antibiotics in bacteria, *Science*, 2011, **334**(6058), 986–990, DOI: 10.1126/science.1209855.

10 H. Zhang, M. Zhu, D. Jiang, X. Xue, J. Zhang, G. Zhang, *et al.*, Ultrafast response fluorescent probe with red-emission for monitoring hydrogen sulfide in vivo and in vitro, *J. Photochem. Photobiol., A*, 2019, **382**, 111974, DOI: 10.1016/j.jphotochem.2019.111974.

11 C. W. Huang, M. E. Walker, B. Fedrizzi, R. C. Gardner and V. Jiranek, Hydrogen sulfide and its roles in Saccharomyces cerevisiae in a winemaking context, *FEMS Yeast Res.*, 2017, **17**(6), fox058, DOI: 10.1093/femsyr/fox058.

12 D. Vojtovič, L. Luhová and M. Petřivalský, Something smells bad to plant pathogens: Production of hydrogen sulfide in plants and its role in plant defence responses, *J. Adv. Res.*, 2021, **27**, 199–209, DOI: 10.1016/j.jare.2020.09.005.

13 M. Zheng, Y. Cheng, X. Zhang, H. Liu, H. Xu, X. Dai, *et al.*, Atomic Ru Species Driven SnO_2-Based Sensor for Highly Sensitive and Selective Detection of H_2S in the ppb-Level, *ACS Sens.*, 2025, **10**(2), 1093–1104.

14 W. Van Genechten, L. Demuyser, S. Duwé, W. Vandenberg, P. Van Dijck and P. Dedecker, Photochromic fluorophores enable imaging of lowly expressed proteins in the autofluorescent fungus Candida albicans, *mSphere.*, 2021, **6**(2), e00146–e00121, DOI: 10.1128/msphere.00146-21.

15 T. Mourer, C. d'Enfert and S. Bachellier-Bassi, Use of the fluorescent dye Thioflavin T to track amyloid structures in the pathogenic yeast Candida albicans, *npj Biofilms Microbiomes*, 2023, **9**, 46, DOI: 10.1038/s41522-023-00332-6.

16 L. Feng, Q. Yan, B. Zhang, X. Tian, C. Wang, Z. Yu, *et al.*, Ratiometric fluorescent probe for sensing Streptococcus mutans glucosyltransferase, a key factor in the formation of dental caries, *Chem. Commun.*, 2019, **55**(24), 3548–3551, DOI: 10.1039/c9cc00440h.

17 Z. Tian, Q. Yan, L. Feng, S. Deng, C. Wang, J. Cui, *et al.*, A far-red fluorescent probe for sensing laccase in fungi and its application in developing an effective biocatalyst for the biosynthesis of antituberculous dicoumarin, *Chem. Commun.*, 2019, **55**(27), 3951–3954, DOI: 10.1039/C9CC01579E.

18 F. Yan, X. Zhao, R. Li, X. Han, Q. Yan, L. Feng, *et al.*, High-throughput fluorescent screening of thioredoxin reductase

inhibitors to inhibit Mycobacterium tuberculosis, *Chin. Chem. Lett.*, 2024, **35**, 108504, DOI: 10.1016/j.cclet.2023.108504.

19 G. Ji, T. Zheng, X. Gao and Z. Liu, A highly selective turn-on luminescent logic gates probe based on post-synthetic MOF for aspartic acid detection, *Sens. Actuators, B*, 2019, **284**, 91–95, DOI: 10.1016/j.snb.2018.12.114.

20 C. Liu, J. Pan, S. Li, Y. Zhao, L. Y. Wu, C. E. Berkman, *et al.*, Capture and visualization of hydrogen sulfide by a fluorescent probe, *Angew. Chem., Int. Ed.*, 2011, **50**(44), 10327–10329, DOI: 10.1002/anie.201104305.

21 Q. Zhao, F. Huo, Y. Zhang, Y. Wen and C. Yin, HS^- induced thiolysis reaction to regulate UV- and fluorescence spectra change and their bioimaging in living cells, *Spectrochim. Acta, Part A*, 2019, **215**, 297–302, DOI: 10.1016/j.saa.2019.02.096.

22 M. D. Hammers, M. J. Taormina, M. M. Cerda, L. A. Montoya, D. T. Seidenkranz, R. Parthasarathy, *et al.* A bright fluorescent probe for H_2S enables analyte-responsive, 3D imaging in live zebrafish using light sheet fluorescence microscopy, *J. Am. Chem. Soc.*, 2015, **137**(32), 10216–10223, DOI: 10.1021/jacs.5b04196.

23 V. S. Lin, A. R. Lippert and C. J. Chang, Azide-based fluorescent probes: Imaging hydrogen sulfide in living systems, *Methods Enzymol.*, 2015, **554**, 63–80, DOI: 10.1016/bs.mie.2014.11.011.

24 J. Men, X. Yang, H. Zhang and J. Zhou, A near-infrared fluorescent probe based on nucleophilic substitution–-cyclization for selective detection of hydrogen sulfide and bioimaging, *Dyes Pigm.*, 2018, **153**, 206–212, DOI: 10.1016/j.dyepig.2018.01.054.

25 R. Kaushik, A. Ghosh and D. A. Jose, Recent progress in hydrogen sulphide (H_2S) sensors by metal displacement approach, *Coord. Chem. Rev.*, 2017, **347**, 141–157, DOI: 10.1016/j.ccr.2017.07.003.

26 K. Sasakura, K. Hanaoka, N. Shibuya, Y. Mikami, Y. Kimura, T. Komatsu, *et al.* Development of a highly selective fluorescence probe for hydrogen sulfide, *J. Am. Chem. Soc.*, 2011, **133**(45), 1803–1805, DOI: 10.1021/ja107614c.

27 D. Jose, R. Sakla, N. Sharma, S. Gadiyaram, R. Kaushik and A. Ghosh, Sensing and bioimaging of the gaseous signaling molecule hydrogen sulfide by near-infrared fluorescent probes, *ACS Sens.*, 2020, **5**(11), 3365–3391, DOI: 10.1021/acssensors.0c01491.

28 M. J. Frisch, G. W. Trucks, H. B. Schlegel, G. E. Scuseria, M. A. Robb, J. R. Cheeseman, *et al.*, *Gaussian 16 Revision C.01*, Gaussian Inc., Wallingford, CT, 2016.

29 W. W. Stewart, Synthesis of 3,6-disulfonated 4-aminonaphthalimides, *J. Am. Chem. Soc.*, 1981, **103**(25), 7615–7620, DOI: 10.1021/ja00415a033.

30 M. F. Braña, J. M. Castellano, A. M. Sanz and C. M. Roldán, Synthesis and cytostatic activity of benzo[*de*]isoquinolin-1,3-diones, *Eur. J. Med. Chem.*, 1981, **16**(3), 207–212.

31 H. Tian, J. Gan, K. Chen, J. He, Q. L. Song and X. Y. Hou, Positive and negative fluorescent imaging induced by naphthalimide polymers, *J. Mater. Chem.*, 2002, **12**(5), 1262–1267.

32 I. Grabchev and J. M. Chovelon, Synthesis and functional properties of green fluorescent poly(methylmethacrylate) for use in liquid crystal systems, *Polym. Adv. Technol.*, 2003, **14**(9), 601–608.

33 X. Poteau, A. I. Brown, R. G. Brown, C. Holmes and D. Matthew, Fluorescence switching in 4-amino-1,8-naphthalimides: "on–off–on" operation controlled by solvent and cations, *Dyes Pigm.*, 2000, **47**(1–2), 91–105.

34 L. Jia, Y. Zhang, X. Guo and X. Qian, A novel chromatism switcher with double receptors selectively for Ag^+ in neutral aqueous solution: 4,5-diaminoalkeneamino-N-alkyl-1,8-naphthalimides, *Tetrahedron Lett.*, 2004, **45**(20), 3969–3973.

35 W. Zhu, M. Hu, R. Yao and H. Tian, A novel family of twisted molecular luminescent materials containing carbazole unit for single-layer organic electroluminescent devices, *J. Photochem. Photobiol., A*, 2003, **154**(2–3), 169–177.

36 I. Grabchev, I. Moneva, V. Bojinov and S. Guittonneau, Synthesis and properties of fluorescent 1,8-naphthalimide dyes for application in liquid crystal displays, *J. Mater. Chem.*, 2000, **10**(6), 1291–1296.

37 Y. Gu, M. Wang, Y. Nan, G. Yu, Y. Lu, Z. Liu, *et al.*, A photochromic salicylhydrazide based on perylene diimide and its application for ion sensor probes, *J. Lumin.*, 2021, **235**, 118416, DOI: 10.1016/j.jlumin.2021.118416.

38 S. Saha and A. Samanta, Influence of the structure of the amino group and polarity of the medium on the photophysical behavior of 4-amino-1,8-naphthalimide derivatives, *J. Phys. Chem. A*, 2002, **106**(18), 4763–4771, DOI: 10.1021/jp013287a.

39 L. Michels, A. Richter, R. K. Chellappan, H. I. Røst, A. Behsen, K. H. Wells, *et al.*, Electronic and structural properties of the natural dyes curcumin, bixin, and indigo, *RSC Adv.*, 2021, **11**(23), 14169–14177, DOI: 10.1039/d0ra08474c.

40 C. Zhao, L. Mendive-Tapia and M. Vendrell, Fluorescent peptides for imaging of fungal cells, *Arch. Biochem. Biophys.*, 2019, **661**, 187–195.

41 L. Mukaremera, K. K. Lee, H. M. Mora-Montes and N. A. R. Gow, Candida albicans yeast, pseudohyphal, and hyphal morphogenesis differentially affects immune recognition, *Front. Immunol.*, 2017, **8**, 629, DOI: 10.3389/fimmu.2017.00629.

42 S. M. Noble, B. A. Gianetti and J. N. Witchley, Candida albicans cell-type switching and functional plasticity in the mammalian host, *Nat. Rev. Microbiol.*, 2017, **15**(2), 96–108, DOI: 10.1038/nrmicro.2016.157.

43 M. Gulati and C. J. Nobile, Candida albicans biofilms: Development, regulation, and molecular mechanisms, *Microbes Infect.*, 2016, **18**(5), 310–321, DOI: 10.1016/j.micinf.2016.01.002.

44 A. D. S. Dantas, K. K. Lee, I. Raziunaite, K. Schaefer, J. Wagener, B. Yadav, *et al.*, Cell biology of Candida albi-

cans–host interactions, *Curr. Opin. Microbiol.*, 2016, **34**, 111–118, DOI: 10.1016/j.mib.2016.08.006.

45 A. J. P. Brown, G. D. Brown, M. G. Netea and N. A. R. Gow, Metabolism impacts upon Candida immunogenicity and pathogenicity at multiple levels, *Trends Microbiol.*, 2014, **22**(12), 614–622, DOI: 10.1016/j.tim.2014.07.002.

46 S. X. Guo, G. F. Yao, H. R. Ye, J. Tang, Z. Q. Huang, F. Yang, *et al.*, Functional characterization of a cystathionine β-synthase gene in sulfur metabolism and pathogenicity of Aspergillus niger in pear fruit, *J. Agric. Food Chem.*, 2019, **67**(14), 3989–3996, DOI: 10.1021/acs.jafc.9b00325.

47 B. L. Gómez and J. D. Nosanchuk, Melanin and fungi, *Curr. Opin. Infect. Dis.*, 2003, **16**(2), 91–96.

48 M. J. Butler and A. W. Day, Fungal melanins: a review, *Can. J. Microbiol.*, 1998, **44**(12), 1115–1136.